

ORIGINAL ARTICLE

Towards a comprehensive understanding of FeCo coated with N-doped carbon as a stable bi-functional catalyst in acidic media

Seung Hyo Noh¹, Min Ho Seo², Joonhee Kang³, Takeyoshi Okajima¹, Byungchan Han⁴ and Takeo Ohsaka¹

The identification and development of efficient catalysts made of non-precious materials for oxygen reduction reaction (ORR) are essential for the successful operation of a wide range of energy devices. This study provides evidence that earth-abundant nanoparticles of transition metals encapsulated in a nitrogen-doped carbon shell (M@N-C, M = Fe, Co, Ni, Cu or Fe alloys) are promising catalysts in acidic solutions. By density functional theory calculations and experimental validations, we quantitatively propose a method of tuning the ORR activity of M@N-C by controlling the nitrogen-doping level, the thickness of the N-C shells and binary alloying. FeCo@N-C/KB was chosen as the best ORR catalyst because of its onset and half-wave potentials of 0.92 and 0.74 V vs a reversible hydrogen electrode (RHE), respectively, and its excellent durability. Furthermore, FeCo@N-C/KB possesses a high activity for the hydrogen evolution reaction (HER; -0.24 V vs RHE at -10 mA cm⁻²), thus demonstrating that it is a good bi-functional ORR and HER catalyst in acidic media.

NPG Asia Materials (2016) 8, e312; doi:10.1038/am.2016.142; published online 23 September 2016

INTRODUCTION

Oxygen electrochemistry has a central role in a wide range of devices used for the generation of energy and fuels. For instance, oxygen reduction and evolution reactions (ORR and OER) are essential for the operation of proton exchange membrane fuel cells,^{1,2} metal-air batteries³ and photovoltaic cells (used for water splitting).

However, ORR has notoriously been known to be sluggish in most electrochemical systems harvesting oxygen to produce renewable energies, thus hindering the design of highly efficient ORR catalysts. Conventional Pt-based nanocatalysts have been intensively studied and optimized to enhance ORR activity, and they are currently the most efficient ORR catalyst materials. Their high material cost and electrochemical instability in acidic solution, however, strongly drives the development of alternatives to Pt. Over the past few decades, studies have sought to achieve this goal, but the alternatives investigated have not been commercialized yet, owing to either their electrochemical instability or their low ORR activity in acidic media.^{2,4-6}

Recent progress in the use of non-precious carbon-based catalysts for ORR is notable because these materials not only are much cheaper than Pt-based alloys but also are stable for prolonged periods. Furthermore, the catalytic properties of carbon-based materials can be well tuned by simple thermo-chemical treatments.^{7,8} For example, nitrogen-doped graphene (N-Gr) has

been reported to be comparable to or even better than Pt in ORR catalysis in alkaline media.^{9,10}

To date, carbon-based catalysts have largely been designed in the form of either macrocyclic structures (such as polyaniline-Fe-C (PANI-Fe-C) and PANI-Co-C) for use in acidic media^{1,8,11,12} or metal oxide particles on reduced graphene oxide (such as Co₃O₄/rGO and Mn₃O₄/rGO) for alkaline media.^{7,13,14} Designing active and stable ORR catalysts is more challenging for acidic media than for alkaline media with regard to both the electrochemical stability and ORR activity. Although several materials have been found to have activity in acidic electrolytes in laboratory experiments, the underlying mechanism is poorly understood. For instance, in the macrocyclic materials (that is, PANI-M-C and phthalocyanine-M^{6,15-18}), Fe has been observed to be at the center of the molecules, but the exact location of the active site is still under debate.

In contrast, metallic nanoparticles encapsulated in N-doped carbon shells (M@N-C_{shells}), such as Fe₃C@N-C or Fe@Pod,¹⁹⁻²² demonstrate superior ORR activity and electrochemical stability in acidic media. This concept of encapsulation has been proposed to simultaneously overcome the conventional limits on the two exclusive properties of electrochemical stability²³ and ORR activity. Because the encapsulated materials are configured as core-shell structures, it is of great interest to determine the role of the core metal in ORR catalysis.

¹Department of Electronic Chemistry, Interdisciplinary Graduate School of Science and Engineering, Tokyo Institute of Technology, Midori-ku, Japan; ²Hydrogen & Fuel Cell Center for Industry, Academy, and Laboratories, New & Renewable Energy Research Division, Korea Institute of Energy Research (KIER), Buan-gun, Korea; ³Department of Energy Systems Engineering, DGIST, Daegu, Korea and ⁴Department of Chemical and Biomolecular Engineering, Yonsei University, Seoul, Korea
Correspondence: Professor B Han, Department of Chemical and Biomolecular Engineering, Yonsei University, 50 Yonsei-ro, Seodaemun-gu, Seoul 03722, Korea.
E-mail: bchan@yonsei.ac.kr

or Professor T Ohsaka, Department of Electronic Chemistry, Interdisciplinary Graduate School of Science and Engineering, Tokyo Institute of Technology, 4259-G1-5 Nagatsuta, Midori-ku, Yokohama 226-8502, Japan.
E-mail: ohsaka.t.aa@m.titech.ac.jp

Received 22 April 2016; revised 4 July 2016; accepted 20 July 2016

Previously, using first-principles density functional theory calculations,^{24,25} we have elucidated the role of three-dimensional transition metals (Ni, Co and Cu) in supporting N-doped carbon layers (N–C/M) in ORR catalysis. Cu@N–C shows a much better ORR activity (with an onset potential (E_{onset}) of 0.94 V and a half-wave potential ($E_{1/2}$) of 0.83 V vs a reversible hydrogen electrode (RHE)) than pure Cu metal and N–C, thus suggesting that the Cu core substantially influences the electronic structure of N–C shells. Cu@N–C also shows high durability in alkaline media, with only a 20 mV negative shift in the $E_{1/2}$ even after 3000 potential cycles between 0.6 and 1.0 V (vs RHE). It has been proposed that the ORR activity may be optimized by controlling the shell thickness of N–C through CO₂ oxidation,²⁶ a possibility consistent with the results of previous experiments.²⁷

In this study, we extensively used density functional theory calculations and experimental characterizations to understand how the nitrogen-doping level, alloying element and shell thickness of the M@N–C catalyst influence ORR catalysis in a 0.5 M H₂SO₄ acidic solution. Using FeM@N–C as a prototype model, we sought to identify the best alloying element (M) to Fe by screening chemical elements such as Co, Ni and Cu. In addition, we calculated and experimentally analyzed the catalytic performance of the structures in the hydrogen evolution reaction (HER) to evaluate the possibility of using them as bi-functional catalysts in acidic media.

MATERIALS AND METHODS

Catalyst synthesis

Fe@N–C. Iron(III) nitrate nonahydrate (Fe(NO₃)₃•9H₂O, 200 mg), glucose (C₆H₁₂O₆, 200 mg) and ammonium sulfate ((NH₄)₂SO₄, 600 mg) were used as the precursors of iron, carbon and nitrogen, respectively. The precursors were mixed with 3 ml of Milli-Q water and ultrasonicated for 10 min. The mixtures were dried on an alumina boat for 2 h at 100 °C under vacuum. The dried solid material was placed in a quartz tube and annealed at 1000 °C for 1 h under Ar gas flow. The powder product was then ground and treated in 25% HCl at 90 °C for 4 h to eliminate metal residues. After filtering with Milli-Q water to remove metal ions, the sample was dried at 80 °C for 30 min under vacuum.

Fe@C or N–C. All of the preparation processes followed the procedure for Fe@N–C, but ammonium sulfate and iron nitrate nonahydrate were not used in the preparation of the Fe@C and N–C catalysts, respectively.

FeCo@N–C and FeCo@N–C/KB. Fe(NO₃)₃•9H₂O (150 mg), Co(NO₃)₂•6H₂O (36 mg), glucose (200 mg) and ammonium sulfate (600 mg) were used as the precursors of iron, cobalt and nitrogen, respectively, and the overall preparation process was identical to that for Fe@N–C. The prepared FeCo@N–C (15 mg) was mixed with acid-treated (36% HCl for 18 h) Ketjen black (2.5 mg, EC-600 JD, Lion Specialty Chemicals, Tokyo, Japan) in water, and then the mixture was dried. The obtained powder was treated again at 1000 °C for 1 h under Ar flow.

Electrochemical analysis

Electrochemical measurements were carried out in a three-electrode electrochemical cell with an ALS/CH Instruments 760Ds electrochemical analyzer (CH Instruments, Austin, TX, USA). Rotating disk electrode voltammetric measurements were performed at a scan rate of 5 mV s⁻¹ with a rotation speed of 900 r.p.m. in N₂- or O₂-saturated 0.5 M H₂SO₄. The counter and reference electrodes were a graphite plate and a Ag|AgCl|KCl_(saturated) electrode, respectively. For the working electrode, a glassy carbon electrode was modified by loading with various catalysts such as FeCo@N–C/KB and Pt/C.

Characterization

The following techniques were used to characterize the bulk and surface structures of different catalysts: high-angle annular dark-field scanning transmission electron microscopy (JEOL JEM-2100 LaB₆, JEOL, Tokyo, Japan) at 200 kV, energy-dispersive X-ray spectroscopy (JEOL JED-2300, JEOL), X-ray diffraction (with an Ultima IV X-ray diffractometer, Rigaku, Tokyo, Japan)

using Cu-K α radiation ($\lambda=1.5418$ Å) at 40 kV and 40 mA, and X-ray photoelectron spectroscopy (with a JEOL JPS-9010MC (JEOL) and a Mg-K α (1253.6 eV) source).

Computational details

First-principles density functional theory calculations were carried out using the Vienna Ab-initio Simulation Package.²⁸ The interaction of the core electrons was replaced by the Projector Augmented Wave pseudo-potential.²⁹ To describe the properties of the magnetic materials such as Co, Ni and Fe, spin polarization was considered in all calculations. Van der Waals interactions were considered, and plane wave basis functions were expanded with a cutoff energy of 520 eV. Calculations were continued until the energy for the ionic relaxation step converged within 1×10^{-4} eV. Models for M@N–C nanoparticles included a vacuum size of ~ 10 Å to preclude interactions among image clusters. The gamma-point scheme was applied with a $1 \times 1 \times 1$ mesh. The bulk surface structure (N–C/metal or bulk N–C) was calculated with periodic boundary conditions and a gamma-point mesh of $5 \times 5 \times 1$, which also included a 10 Å vacuum perpendicular to the surface. Moreover, the bulk surface consisted of four carbon layers with a 3×3 supercell and atoms in the bottom-most two layers in the N–C/metal, which were fixed at their bulk positions (Supplementary Figure S1).

Equations

$$E_{\text{dop}}^{\text{nth}} = E(C_{m-n}N_nM_l) - E(C_{m+1-n}N_{n-1}M_l) + E(C_1)_{\text{bulk}} - \frac{1}{2}E(N_2) \quad (1)$$

where $E_{\text{dop}}^{\text{nth}}$ is the nitrogen-doping energy of the n th nanoparticle. $E(C_{m-n}N_nM_l)$, $E(C_{m+1-n}N_{n-1}M_l)$, $E(C_1)_{\text{bulk}}$ and $E(N_2)$ are the ground-state energies of the n th N-doped particle, the $(n-1)$ th N-doped particle, and one atom in the bulk graphite and nitrogen molecule, respectively. The numbers for the total carbon atoms, doped nitrogen atoms and metal atoms are denoted m , n and l , respectively. In our model, the total numbers of carbon and nitrogen atoms in the first and the second layers were 240 and 720, respectively. The number of metal atoms (l) was 55.

$$E_{\text{bind}}^{\text{O}} = - (E_{\text{catal-O}} - E_{\text{catal}} - E_{\text{O}}) \quad (2)$$

where, $E_{\text{bind}}^{\text{O}}$ is the binding energy of atomic oxygen. The ground-state energies of the oxygen adsorbed catalyst, pure catalyst and oxygen atom are denoted as $E_{\text{catal-O}}$, E_{catal} , and E_{O} , respectively.

$$\bar{E}_{\text{form}}(\text{Fe}_n\text{M}_m) = \bar{E}(\text{Fe}_n\text{M}_m) - x\bar{E}(\text{M}_{n+m}) - (1-x)\bar{E}(\text{Fe}_{n+m}) \quad (3)$$

where, $\bar{E}_{\text{form}}(\text{Fe}_n\text{M}_m)$ is the formation energy of FeM binary alloys. $\bar{E}(\text{Fe}_n\text{M}_m)$, $\bar{E}(\text{M}_{n+m})$ and $\bar{E}(\text{Fe}_{n+m})$ represent the ground-state energies per atom of the FeM alloy, pure Fe and M (M = Cu, Ni and Co), respectively. The value of x represents the composition of an alloying M metal. The numbers of atoms of Fe and M are indicated by n and m , respectively.

$$E_{\text{bind}}^{\text{H}} = E_{\text{catal-H}} - E_{\text{catal}} - \frac{1}{2}E_{\text{H}_2} \quad (4)$$

where, $E_{\text{bind}}^{\text{H}}$ is the binding energy of H₂ on the surface of the catalysts. $E_{\text{catal-H}}$, E_{catal} and E_{H_2} denote the ground-state energies of hydrogen atom in the adsorbed catalyst, pure catalyst and H₂ gas, respectively.

$$\Delta G_{\text{H}^+} = E_{\text{bind}}^{\text{H}} + \Delta ZPE + T\Delta S \quad (5)$$

where, ΔG_{H^+} is the Gibbs free energy of hydrogen atom adsorption on the catalysts. ZPE, T and S are the zero-point energy, temperature and entropy, respectively. In our study, $\Delta ZPE + T\Delta S$ was approximated as 0.24 eV in accordance with the previous reports.^{30,31} Accordingly, ΔG_{H^+} was calculated by $\Delta G_{\text{H}^+} = E_{\text{bind}}^{\text{H}} + 0.24$ eV.

RESULTS AND DISCUSSION

Nitrogen-doping level and ORR activity

Transmission electron microscopy images of FeCo@N–C and FeCo@N–C supported by Ketjen black (FeCo@N–C/KB) are shown in Figure 1a–c. The FeCo nanoparticles depicted in Figure 1a and b

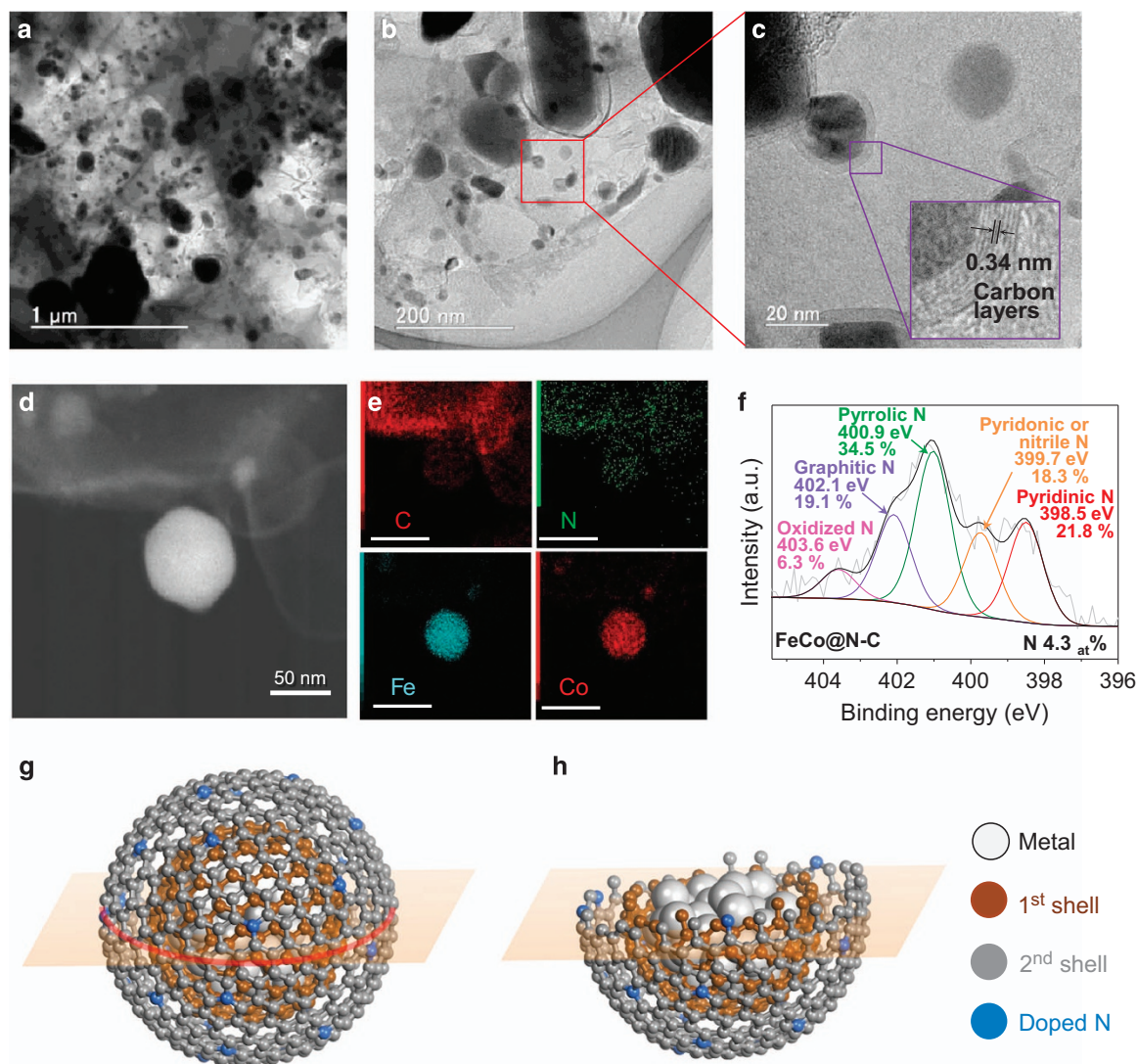


Figure 1 Structural analysis of FeCo@N-C and theoretical model of M@N-C catalysts. Transmission electron microscopy images of (a) FeCo@N-C and (b, c) FeCo@N-C/KB catalysts. (d, e) Elemental mapping of C, N, Fe and Co by energy-dispersive X-ray spectroscopy (scale bars = 100 nm). (f) Core level N 1s X-ray photoelectron spectroscopy spectra of FeCo@N-C catalyst. (g) Illustration of metal@N-C nanoparticle and (h) cross-sectional view of metal@N-C.

have various sizes, and Figure 1c shows particles of ~ 30 nm. The particles of FeCo@N-C/KB are coated by N-doped carbon layers with an interlayer distance of 0.34 nm (Figure 1c). The elemental mapping of FeCo@N-C indicates that C and N completely exist along with the catalyst, and Fe and Co atoms are partially visible in Figure 1d and e. The X-ray photoelectron spectroscopy analysis of FeCo@N-C (Figure 1f) shows a relatively high-nitrogen-doping level of 4.3 at%.^{32,33} Based on the deconvolution analysis, we identified that pyrrolic N is dominant over a variety of other functional N groups. The atomic ratios of the pyrrolic, pyridinic, graphitic, oxidized and pyridonic or nitrile N were evaluated as 34.5%, 21.8%, 19.1%, 6.3% and 18.3%, respectively.^{32,33} In contrast, the pyrrolic N in the Fe@N-C has an extremely strong bonding with oxygen ($E_b = 7.34$ eV in Supplementary Figure S3), thus suggesting extremely slow kinetics for ORR. Instead, the binding energy of the M@N-C with O was tuned with regard to graphitic N by controlling the electronic structure of the nearest carbon with core metals, thus indicating that the binding energy of O on the Fe@N-C is 4.45 eV, which is similar to the binding energy of 4.46 eV on the Pt surface. Hence, the graphitic N in the model would function as the

active site, but the pyrrolic N would not be the active site because in this case a larger energy is required to activate oxygen reduction, as mentioned above. X-ray diffraction analysis of FeCo@N-C was discussed in Supplementary Figure S10.

Theoretical models were set up in accordance with the experimental observations, and front and cross-sectional views of the M@N-C nanoparticle are shown (Figure 1g and h; Supplementary Figure S3).

The nitrogen-doping level (D_N) in low-dimensional carbon- or graphene-based catalysts substantially affects ORR efficiency.³⁴ We studied the oxygen binding energies on M@N-C (M: Cu, Fe, Co and Ni) nanocatalysts typically at 0, 0.42, 1.67, 3.33 and 5 at.% (Figure 2d), as previously reported.^{19,20} The thermodynamic feasibility of the N doping was estimated by density functional theory calculations of the energy required to replace C with N using equation (1).

The doping site of N was searched in a stepwise manner. First, from local symmetry, we allocated N to three carbons as N_α , N_β and N_γ (Figure 2a), and the calculated doping energies in Cu@N-C, Fe@N-C, Co@N-C and Ni@N-C are shown in Supplementary Table S1a (Supplementary Information). The N_α in a pentagonal symmetry is

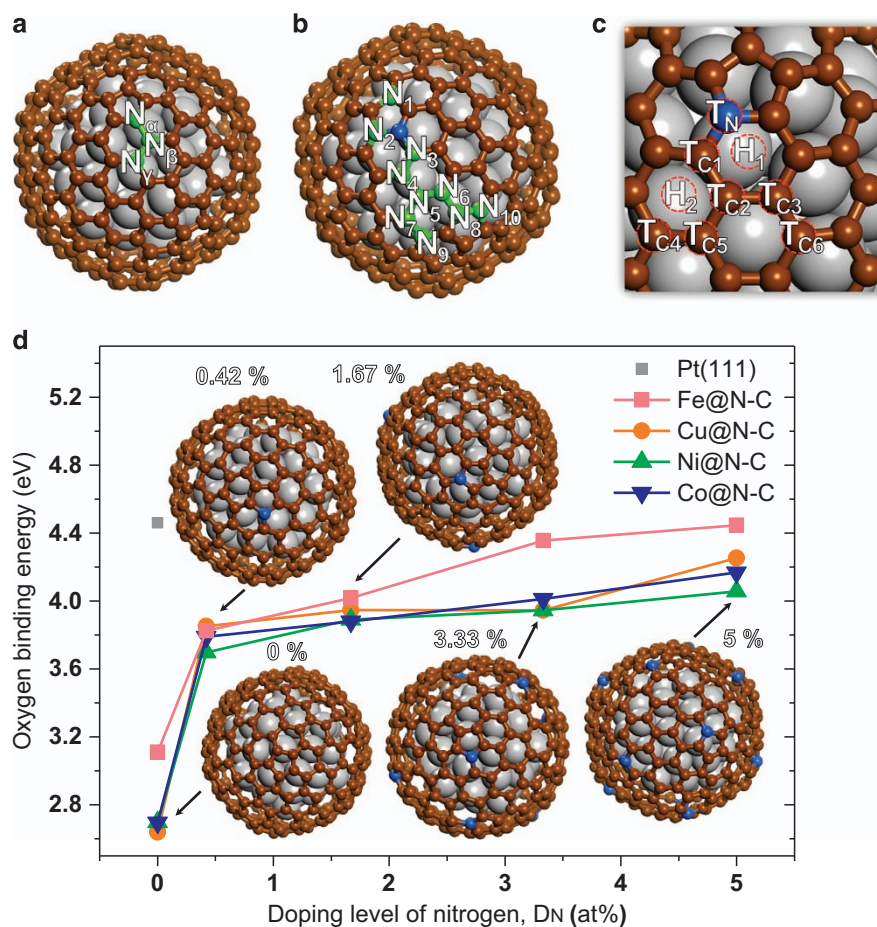


Figure 2 Nitrogen-doping model and oxygen binding energy on M@N-C. (a) First nitrogen-doping positions, typically N_α , N_β and N_γ . (b) Second nitrogen-doping positions from N_1 to N_{10} . (c) Oxygen binding sites on M@N-C (refer to Supplementary Table S1c for the oxygen binding energy with each oxygen position). (d) Oxygen binding energies on M@N-C ($M = \text{Fe, Cu, Ni}$ and Co) as a function of D_N , typically 0, 0.42, 1.67, 3.33 and 5 at.%. The oxygen binding energy (4.46 eV) on Pt(111) is marked for comparison with those on M@N-C.

energetically most favorable, regardless of the core metal used. As the next doping sites, N_8 and N_{10} were also identified (Supplementary Table S1b) with the local pentagonal symmetry. Thus, we found a rule that the farther the doping site from already doped sites, the easier the N doping (that is, $N_9 < N_7 < N_6 < N_5 < N_4 < N_3$; Figure 2b). Notably, the doping energies in N_α , N_β and N_γ are all positive, thus suggesting that heat treatment may be necessary for the N doping.^{35,36}

In this study, we used the well-known electronic structure theory^{37–41} to describe the ORR catalytic activity of the M@N-C nanocatalysts, which posits that the binding energy of a key intermediate (that is, O in our study) with the catalyst surface controls the overall ORR efficiency. The theory has roots in the strain energy and ligand-field effects,^{3,42} essentially proposing that the optimum catalyst should bind to O by ca. 0.2 eV less than Pt (4.46 eV from our calculation). Thus, we calculated binding energies of O at various binding sites in M@N-C catalysts (at $D_N = 5$ at.%) using equation (2), as shown in Figure 2c (Supplementary Table S1c). T_{C1} is the strongest adsorption site for O, whereas T_N is the weakest one. The binding energy increases with D_N when $D_N < 5$ at.%, regardless of the core metals (Figure 2d). Binding energies of O in M@C ($D_N = 0\%$) were too low (2.64 ~ 3.11 eV) for ORR catalysis (Supplementary Figure S12). At $D_N = 5$ at.%, the binding energies in Fe@N-C, Cu@N-C, Co@N-C and Ni@N-C were calculated as 4.45, 4.25, 4.17 and 4.06 eV, respectively. Interestingly, the Fe@N-C binds to O

with approximately the same energy as that for a bulk Pt (111) surface, whereas Cu@N-C, Co@N-C and Ni@N-C catalysts do so with much lower values, thus suggesting that the Fe@N-C nanoparticle may be a promising ORR catalyst as long as other properties such as electrochemical stability can be maintained.

This beneficial enhancement would come from the modified electronic structure, as described in our previous study,²⁴ in which we discovered that the electrons in the core metal are donated to the nearest-neighbored carbon from graphitic N, and then the covalent binding between C and O is strengthened, which has a positive effect of regulating the binding energy with O. Therefore, active sites with high catalysis can be achieved by a suitable selection of inner metals in the M@N-C structure. However, if core metals are not used, the edge sites such as pyridinic and pyrrolic N can be active sites in nitrogen-doped graphene (N-Gr), as reported previously.⁴³ Accordingly, other N-doping types such as pyrrolic or pyridinic N may be associated with an active site in different conditions, for example, conditions with different inner metals, carbon thicknesses and N-doping levels.

Our experimental results showed that FeCo@N-C/KB was the most active catalyst, as depicted in Figure 3a, with an E_{onset} and $E_{1/2}$ of 0.92 and 0.74 V vs RHE, respectively (the E_{onset} and $E_{1/2}$ for commercial Pt/C catalysts are typically 1.02 and 0.82 V vs RHE, respectively). In particular, FeCo@N-C/KB possesses a high graphitic N doping (19.1 at.%) compared with the other catalysts, thus suggesting that the

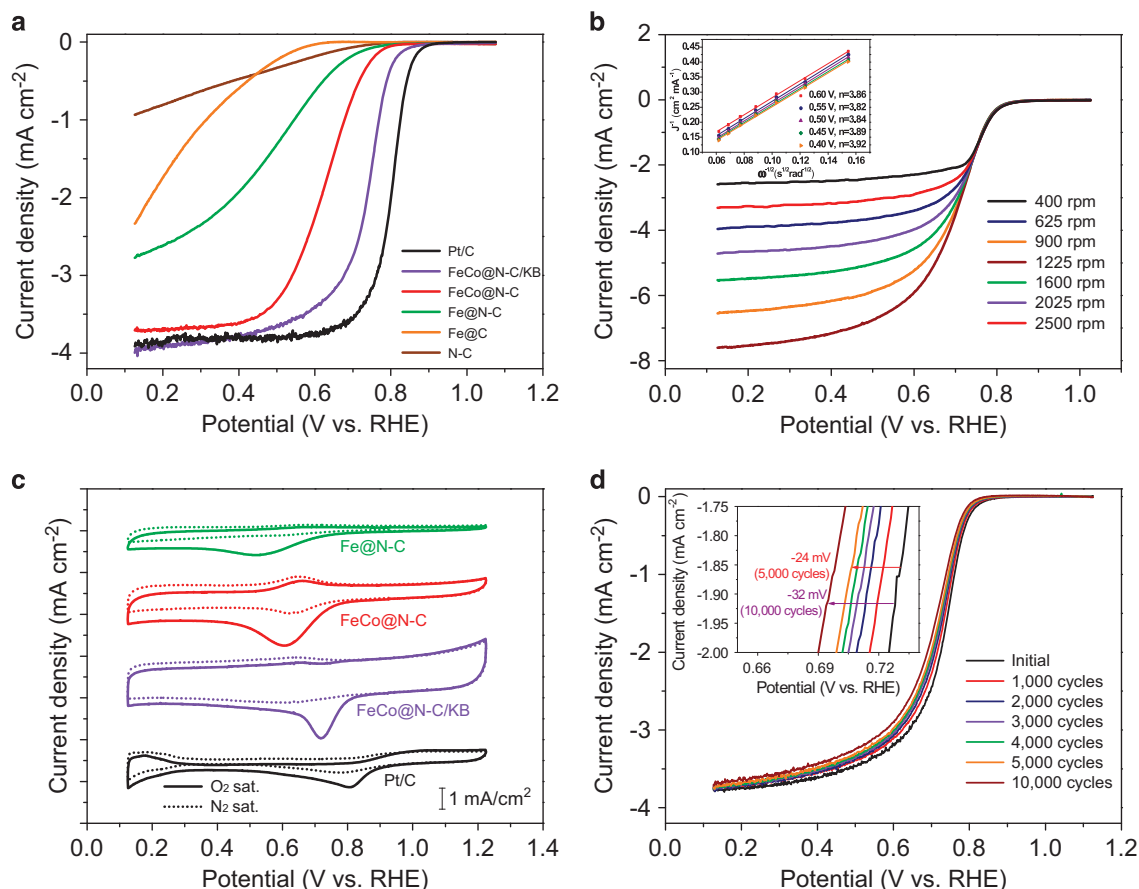


Figure 3 Electrocatalytic ORR performance of M@N-C catalysts. (a) Linear sweep voltammograms for FeCo@N-C, FeCo@N-C/KB, Fe@N-C, Fe@C and Pt/C. The measurements were carried out at 5 mV s^{-1} and 900 r.p.m. in O_2 -saturated $0.5 \text{ M H}_2\text{SO}_4$ solution. The loading amounts of non-precious catalysts and Pt/C were 0.6 mg cm^{-2} and $50 \mu\text{g}_{\text{Pt}} \text{ cm}^{-2}$, respectively. (b) ORR polarization curves of FeCo@N-C/KB nanoparticle at various rotation speeds and Koutecky–Levich plots at various electrode potentials (inset). (c) Cyclic voltammograms of a variety of catalysts at 10 mV s^{-1} . (d) Durability test of FeCo@N-C/KB. The potential scan was repeated between 0.6 and 1.0 V vs RHE at 100 mV s^{-1} in N_2 -saturated $0.5 \text{ M H}_2\text{SO}_4$. RHE, reversible hydrogen electrode.

graphitic N has an essential role as an active site in the ORR. The ORR peak potentials are more positive in the order of FeCo@N-C/KB > FeCo@N-C > Fe@N-C, reflecting their ORR activity (Figure 3c).

The oxidation and reduction peaks in the FeCo@N-C catalyst were observed at $\sim 0.6 \text{ V}$ (vs RHE). As reported by Wu *et al.*,⁸ the peaks may originate from the redox reactions of $\text{Fe}^{3+}/\text{Fe}^{2+}$ and/or quinone/hydroquinone couples, in which the former is due to an impurity contained in the catalyst, whereas the latter is an electroactive functional group usually formed on carbon electrode surfaces. The detailed explanation of this is yet to be clarified.

To understand the role of metal and nitrogen doping in ORR catalysis, the ORR activity of N-C and Fe@C was also examined. Both catalysts have a poor ORR activity compared with the above-mentioned catalysts, thus revealing that both the inclusion of a core side metal and nitrogen doping are necessary to activate the encapsulated catalysts for ORR. Using the Koutecky–Levich equation (Supplementary equations S1 and 2), we estimated the number of the electrons (n) involved in ORR for the FeCo@N-C/KB with varying electrode potentials between 0.4 and 0.6 V (vs RHE), as shown in Figure 3b (inset). The values of n at 0.4, 0.45, 0.5, 0.55 and 0.6 V (vs RHE) were estimated to be 3.92, 3.89, 3.84, 3.82 and 3.86, respectively. Thus, the ORR on the FeCo@N-C/KB can be considered to be close to the ideal $4e^-$ process.

Furthermore, FeCo@N-C/KB showed a high durability in acidic solution; $E_{1/2}$ shifted negatively by only 24 mV, even after 5000 potential cycles at 100 mV s^{-1} were carried out between 0.6 and 1.0 V (vs RHE; Figure 3d).

Thickness of carbon shells for ORR activity

To quantitatively characterize the effect of the carbon shell thickness on the ORR activity, we calculated the oxygen binding energies using a slab model system with N-C layers overlaying the core metals (N-C/M) (Figure 4; Supplementary Figure S1), in which D_{N} was fixed at 5 at.% by considering the experimental validation with $D_{\text{N}} = 4.3$ at.% (Figure 1f).

The N-C/Fe surface with one carbon layer adsorbs O much more strongly than the others. As the carbon thickness increases from one to two atomic layers, the binding energy of O in the N-C/Fe decreases from 4.4 to 4.02 eV. Other core metals (Cu, Co and Ni) overlaid by N-C also showed similar behaviors: the thicker the carbon layer, the less affinity to the binding with O. When carbon shells are three or four layers, the binding energy is close to that of the N-C bulk in N-C/Co and N-C/Ni; however, N-C/Fe and N-C/Cu have higher (stronger) adsorption energies. The difference in the oxygen adsorption energies for the pure metals is as much as 2 eV (Figure 4b; Supplementary Figure S2; Supplementary Table S2), but all the pure

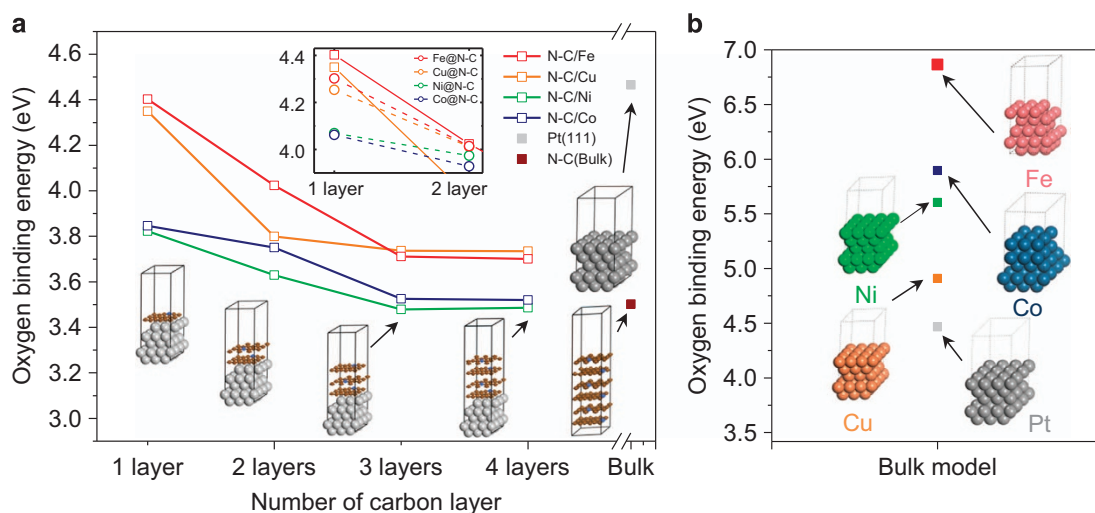


Figure 4 Oxygen binding energy as a function of the number of carbon layer. (a) Oxygen binding energies on N-C/M (Bulk) and M@N-C (nanoparticle, 1.5 nm) as a function of the number of carbon layer, including Pt(111) and N-C (Bulk). (b) Oxygen binding energies on pure bulk metals of Fe, Ni, Co, Cu and Pt.

metals have stronger binding affinities than Pt, hence suggesting lower ORR activity. Thus, it is clear that the thickness of the N-doped carbon shell (layers) has an important role in the O binding energy and ORR activity for bulk N-C/M surfaces, as previously reported.²⁴

In contrast, M@N-C nanoparticles show a relatively small dependence of the oxygen binding energy on the thickness of the carbon layers. For example, the decrease in O binding energies for Fe@N-C with one and two carbon shells is less (~ 0.2 eV) than that (~ 0.38 eV) for N-C/Fe with one and two carbon layers. Therefore, for the same number of carbon layers, nanoparticles encapsulated with N-C shells (~ 20 nm) have better ORR activity than bulk N-C/M surfaces. Furthermore, our calculations predicted that a thinner layer would be better for ORR in M@N-C nanoparticles.^{27,44,45} These tendencies are consistent with previous reports that the thinner layer of carbon leads to higher activity in the FeCo alloy catalyst encapsulated in pod-like carbon nanotubes. Moreover, a particle encapsulated with a single layer of carbon has also been used as a HER and OER catalyst with superior activity.⁴⁴

In other aspects, the heterogeneity of the catalyst structures can be observed for different N-doping levels and varying thicknesses of the carbon layer. To clarify these effects, the oxygen binding energies of different N-doping levels were determined, as shown in Figure 2d, including the effects of different doping levels (0~5%). In addition, ORR activities were investigated by comparing two different particle size regimes of 1.5 nm and the particle size in the bulk material, as shown in Figure 4 in which oxygen binding energies are plotted as a function of the number of carbon layers. Our results indicate that the oxygen binding energies on the N-C/M(bulk) catalysts with more than four layers do not vary substantially (they seem to converge to the oxygen binding energies of the bulk materials). Therefore, we proposed our calculations for particles, specifically for discretely sized particle models, to capture the trend for the effect of the carbon shell thickness on the oxygen binding energy.

Alloying element (FeM catalysts, M = Cu, Ni and Co) and ORR activity

Pt-based binary alloys have often shown a higher ORR activity than pure Pt via their weaker binding energy with O. We applied the same concept to design FeM@N-C (M: Co, Ni and Cu). Using an energy

convex hull diagram,^{30,46,47} we calculated the thermodynamic feasibility of forming binary nanoalloys under encapsulation by N-C shells. We defined the formation energy by equation (3).

Here, x denotes the composition of an alloying element M. Figure 5a–c show energy convex hull diagrams of Fe-based binary nanoalloys (FeCu, FeCo and FeNi). Cu and Ni enable the substitution of Fe sites at a value of x as high as 0.76 (Figure 5a and b; Supplementary Figure S4–5 in Supplementary Information) primarily at the outermost surface of the Fe nanoparticle; these results agree with the previously measured⁴⁸ energy-dispersive X-ray spectroscopy profile for CuFe_{1-x}N_x/C nanoparticle.

However, FeCo nanoparticles show completely different configurations. At $x < 0.07$, Co atoms are not stable on the surface of Fe nanoparticle but stay inside the particle (Figure 5c, Supplementary Figure S6). Co atoms begin to emerge onto the outermost surface at $x > 0.31$. These results can be explained by the surface segregation energy, as shown in Figure 5d, where Cu and Ni atoms segregate on the surface sites of C or D, but a Co resides at B without surface segregation (Supplementary Figure S7; Supplementary Table S3). The surface segregation behavior is closely associated with the surface energy and atomic radius.^{49,50} Because the atomic radii of the alloying elements (Cu, Ni and Co) are very similar, we believe that the surface energy should be more influential: 2.417 (Fe), 1.790 (Cu), 2.380 (Ni) and 2.522 (Co) J m⁻².⁵¹ Cu and Ni have lower surface energies than Fe, thus describing the easier surface segregations of Cu and Ni satisfactorily, whereas Co has a relatively higher surface energy (Figure 5d). Experimentally, the energy-dispersive X-ray spectroscopy profile (Figure 5f) of FeCo@N-C supports the theoretical prediction, as observed from the weak intensity of Co atoms at the outermost positions.

The O binding energy of Fe@N-C is similar to that on bulk Pt(111) and hence its ORR activity is less than the optimized value. For the same reason, the ORR activity of Cu@N-C ($x = 1$) should be better than that of the Pt(111) surface (Figure 5e). Notably, Cu@N-C adsorbs O with an adequate energy. However, the formation of graphitic carbon layers on Cu surface is quite challenging.^{23,38} For example, Nam *et al.*⁴⁸ have noted that Fe catalyzes the crystallization of amorphous carbon into graphite, whereas Cu does not. Hence, we removed Cu@N-C from our list of candidates for good ORR catalysts.

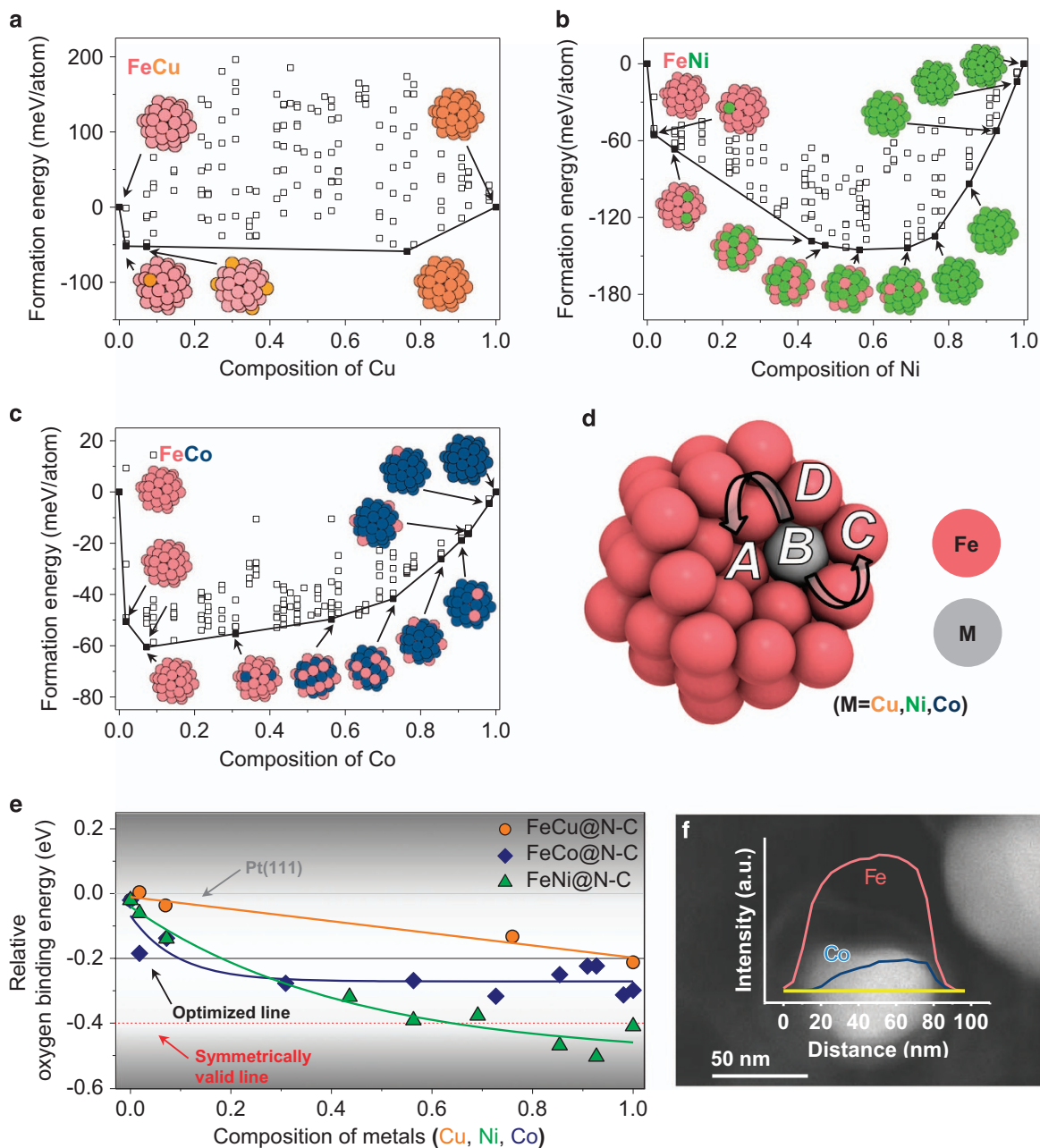


Figure 5 Alloying effect of M@N-C catalysts via density functional theory calculations and experimental observations. Energy convex hulls of (a) FeCu, (b) FeNi and (c) FeCo nanoparticles. (d) Segregation model in FeM nanoparticle. The segregated positions are the core of nanoparticle (A), vertex (C), edge (D) or sublayer (B, not segregated). (e) Relative oxygen binding energies on FeM@N-C nanoparticles as a function of the composition of second metal (M). Oxygen binding energies are represented as $E(\text{FeM@N-C}) - E(\text{Pt(111)})$, where $E(\text{FeM@N-C})$ and $E(\text{Pt(111)})$ are oxygen binding energies on FeM@N-C and Pt(111), respectively. (f) Transmission electron microscopy image and the elemental profile by energy-dispersive X-ray spectroscopy of FeCo@N-C nanoparticle.

To optimize Fe@N-C towards ORR, we tuned the binding energy of O by properly alloying Fe with the Cu, Ni or Co element at various compositions. Figure 5e shows the O binding energy as a function of the composition of the alloying element M in FeM@N-C. FeCu@N-C binds O with the proper energy over a wide range of Cu compositions. However, only a few FeCu@N-C structures were predicted to be stable FeCu alloy structures (Figure 5a), thus making the fine-tuning of the O binding energy challenging. FeNi@N-C shows a variety of O binding energies depending on the Ni composition. At $x < 0.6$, the FeNi@N-C has proper binding energies with O, but they become too low at $x > 0.6$, and converge to that of a pure Ni@N-C. Compared

with FeCu@N-C and FeNi@N-C, FeCo@N-C shows optimal binding energies with O over a wide range of Co compositions, and many stable alloy structures are available (Figure 5c). Thus, we propose that the FeCo@N-C may be very promising for ORR (Supplementary Table S4).

Activity towards HER of FeCo@N-C

In addition to ORR applications, we further studied the activity of M@N-C for HER in acidic medium. As shown in Figure 6a, FeCo@N-C and FeCo@N-C/KB demonstrate much higher HER activity (-0.23 and -0.24 V vs RHE at -10 mA cm^{-2} , respectively)

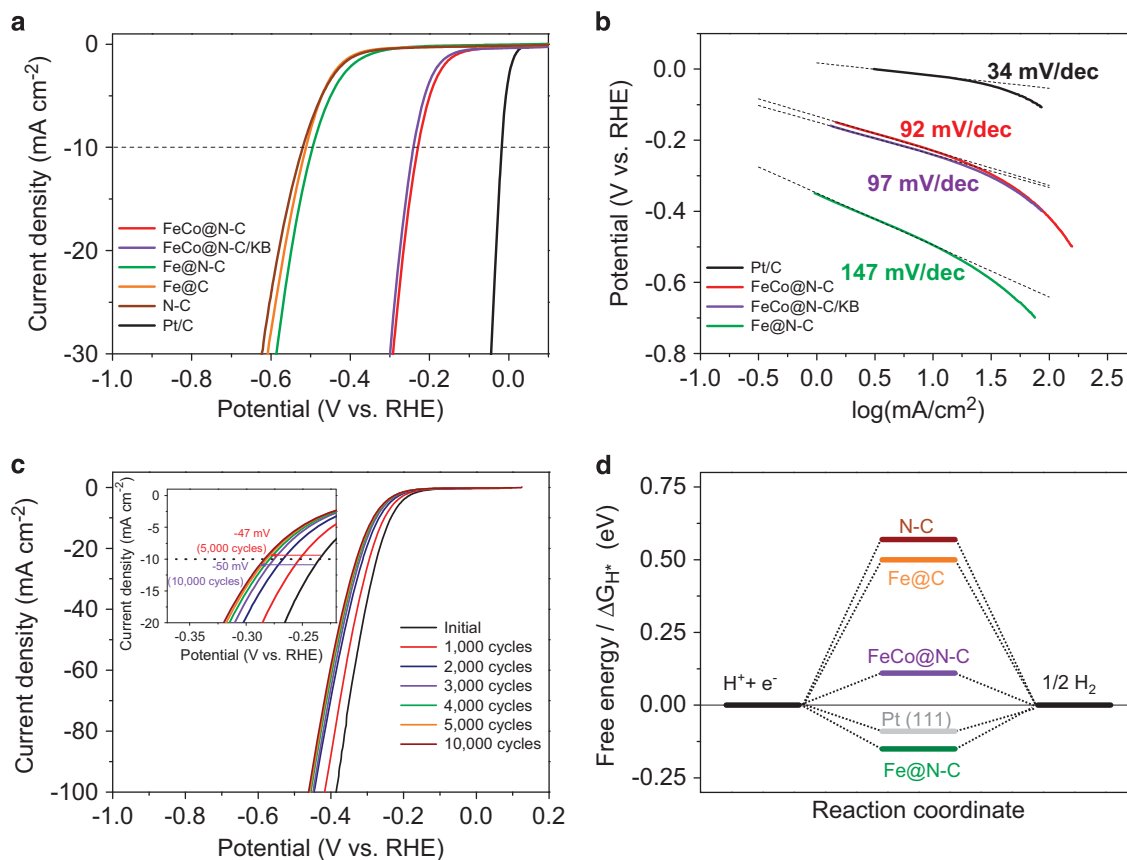


Figure 6 HER performance of different catalysts and their DFT calculations. (a) HER polarization curves for FeCo@N-C, FeCo@N-C/KB, Fe@N-C, Fe@C, N-C and Pt/C in N₂-saturated 0.5 M H₂SO₄ at 5 mV s⁻¹. (b) Tafel plots of FeCo@N-C, FeCo@N-C/KB, Fe@N-C and Pt/C. (c) Durability test of FeCo@N-C/KB. The potential scan was repeated between -0.3 and 0.2 V vs RHE at 100 mV s⁻¹ in N₂-saturated 0.5 M H₂SO₄ under a rotating of 1600 r.p.m. (d) DFT calculations of Gibbs free energies for the adsorption of H on different catalysts including FeCo@N-C ($x=0.85$). A negative free energy means the strong adsorption of H on catalysts by the definition of H adsorption energy (equations (4) and (5)). DFT, density functional theory, RHE, reversible hydrogen electrode.

than Fe@N-C, Fe@C and N-C. To understand the reaction mechanism of HER, we calculated the Tafel slopes, as illustrated in Figure 6b. FeCo@N-C shows a Tafel slope of 92 mV dec⁻¹, thus suggesting that the HER obeys the Volmer–Heyrovsky mechanism (Supplementary equations S4) in contrast to the Volmer–Tafel mechanism (Supplementary equations S5) on Pt/C (~34 mV dec⁻¹). A negative shift of 47 mV in the HER was observed after 5000 potential cycles between -0.3 and 0.2 V vs RHE (Figure 6c), thus demonstrating its high durability.

We also calculated the Gibbs free energies of the intermediates (ΔG_{H^*}), which is the key descriptor of the HER activity for various catalysts,^{52–54} to examine the HER activity of M@N-C catalysts. The value of ΔG_{H^*} for the N-C, Fe@C, Fe@N-C and FeCo@N-C are presented in Figure 6d. By N doping, ΔG_{H^*} significantly decreases, for example, from 0.50 (Fe@C) to -0.15 eV (Fe@N-C) because of the different electron affinities between C and N, thereby inducing heterogeneous electron distribution near the N sites. Alloying Fe with Co enables tuning of the H adsorption energy (0.11 eV), consistently with our experimental results (Figure 6a) as well as previous reports.⁵³

Bao *et al.*⁵⁴ have demonstrated that the thickness of graphene layers in M@N-C catalysts substantially influences the HER activity, and a single-layer graphene shell has the best catalytic activity. Our calculations also predict that the HER activity of FeCo encapsulated by a single-layer graphene shell is comparable to that of Pt/C, which

originates because the H adsorption energy is tuned by the carbon shell thickness in addition to the N-doping treatment.

CONCLUSIONS

Theoretical calculations and experimental validations were integrated for core nanometals encapsulated by N-doped carbon shells (M@N-C) to develop a design concept for determining the best ORR catalyst in acidic media. We thoroughly analyzed the effects of the N-doping level and active N sites, the thickness of the carbon layers, and the binary alloying elements leading to substantially high ORR activity and electrochemical stability. We found that Fe@N-C at $D_N = 5$ at.% adsorbs O with approximately the same energy (4.45 eV) as the bulk Pt(111) surface does, and the oxygen binding energy on Fe-M@N-C can be controlled arbitrarily using N-doping at pentagonal symmetric sites instead of carbon atoms. FeCo@N-C/KB ($E_{onset} = 0.92$ and $E_{1/2} = 0.74$ V vs RHE) was found to be an excellent bi-functional catalyst for HER as well as ORR, with a high durability in acidic solution. These theoretical calculations (the N-doping level, carbon thickness and alloying effect) and experimental validations may facilitate the design of high-performance catalysts for ORR and HER, which are essential electrochemical reactions in a wide range of energy devices.

CONFLICT OF INTEREST

The authors declare no conflict of interest.

ACKNOWLEDGEMENTS

This study was supported by the Ministry of Education, Culture, Sports, Science and Technology (MEXT), Japan and the Global Frontier Program through the Global Frontier Hybrid Interface Materials (GFHIM) of the National Research Foundation of Korea (NRF), which is funded by the Ministry of Science, ICT & Future Planning (grant number 2013M3A6B1078882). This work was partially supported in the New and Renewable Energy R&D Program (20113020030020) under the Ministry of Knowledge Economy, and the framework of Research and Development Program of KIER (B6-2425) from the Korea. Seung Hyo Noh also thanks the Government of Japan for the MEXT scholarship. We thank Material Analysis Suzukake-dai Center, Technical Department, Tokyo Institute of Technology, for X-ray diffraction and transmission electron microscopy measurements. In addition, we are grateful to Takao Gunji and Professor Futoshi Matsumoto for their help in X-ray photoelectron spectroscopy measurements.

Author contributions: TO and BH supervised the experiments and calculations, respectively. SHN and TO carried out the experimental measurements, and MHS performed the data analysis. SHN and JK wrote the paper and performed the theoretical calculations. All the authors discussed the theoretical and experimental results.

- 1 Shao, M. *Electrocatalysis in Fuel Cells* (Springer, 2013).
- 2 Doyle, M., Rajendran, G., Vielstich, W., Gasteiger, H. A. & Lamm, A. *Handbook of Fuel Cells Fundamentals, Technology and Applications*, Vol. 3 (Wiley, 2003).
- 3 Seo, M. H., Park, H. W., Lee, D. U., Park, M. G. & Chen, Z. Design of highly active perovskite oxides for oxygen evolution reaction by combining experimental and ab initio studies. *ACS Catal.* **5**, 4337–4344 (2015).
- 4 Strasser, P., Koh, S., Anniyev, T., Greeley, J., More, K., Yu, C., Liu, Z., Kaya, S., Nordlund, D., Ogasawara, H., Toney, M. F. & Nilsson, A. Lattice-strain control of the activity in dealloyed core-shell fuel cell catalysts. *Nat. Chem.* **2**, 454–460 (2010).
- 5 Stamenkovic, V. R., Mun, B. S., Arenz, M., Mayrhofer, K. J., Lucas, C. A., Wang, G., Ross, P. N. & Markovic, N. M. Trends in electrocatalysis on extended and nanoscale Pt-bimetallic alloy surfaces. *Nat. Mater.* **6**, 241–247 (2007).
- 6 Seo, M. H., Choi, S. M., Lim, E. J., Kwon, I. H., Seo, J. K., Noh, S. H., Kim, W. B. & Han, B. Toward new fuel cell support materials: a theoretical and experimental study of nitrogen-doped graphene. *ChemSusChem* **7**, 2609–2620 (2014).
- 7 Liang, Y., Li, Y., Wang, H., Zhou, J., Wang, J., Regier, T. & Dai, H. Co₃O₄ nanocrystals on graphene as a synergistic catalyst for oxygen reduction reaction. *Nat. Mater.* **10**, 780–786 (2011).
- 8 Wu, G., More, K. L., Johnston, C. M. & Zelenay, P. High-performance electrocatalysts for oxygen reduction derived from polyaniline, iron, and cobalt. *Science* **332**, 443–447 (2011).
- 9 Gong, K., Du, F., Xia, Z., Durstock, M. & Dai, L. Nitrogen-doped carbon nanotube arrays with high electrocatalytic activity for oxygen reduction. *Science* **323**, 760–764 (2009).
- 10 Geng, D., Chen, Y., Chen, Y., Li, Y., Li, R., Sun, X., Ye, S. & Knights, S. High oxygen-reduction activity and durability of nitrogen-doped graphene. *Energy Environ. Sci.* **4**, 760–764 (2011).
- 11 Yan, X.-H. & Xu, B.-Q. Mesoporous carbon material co-doped with nitrogen and iron (Fe–N–C): high-performance cathode catalyst for oxygen reduction reaction in alkaline electrolyte. *J. Mater. Chem. A* **2**, 8617–8622 (2014).
- 12 Wang, M.-Q., Yang, W.-H., Wang, H.-H., Chen, C., Zhou, Z.-Y. & Sun, S.-G. Pyrolyzed Fe–N–C composite as an efficient non-precious metal catalyst for oxygen reduction reaction in acidic medium. *ACS Catal.* **4**, 3928–3936 (2014).
- 13 Menezes, P. W., Indra, A., González-Flores, D., Sahraie, N. R., Zaharieva, I., Schwarze, M., Strasser, P., Dau, H. & Driess, M. High-performance oxygen redox catalysis with multifunctional cobalt oxide nanochains: morphology-dependent activity. *ACS Catal.* **5**, 2017–2027 (2015).
- 14 Liang, Y., Wang, H., Zhou, J., Li, Y., Wang, J., Regier, T. & Dai, H. Covalent hybrid of spinel manganese-cobalt oxide and graphene as advanced oxygen reduction electrocatalysts. *J. Am. Chem. Soc.* **134**, 3517–3523 (2012).
- 15 Artyushkova, K., Kiefer, B., Halevi, B., Knop-Gericke, A., Schlogl, R. & Atanassov, P. Density functional theory calculations of XPS binding energy shift for nitrogen-containing graphene-like structures. *Chem. Commun.* **49**, 2539–2541 (2013).
- 16 Kattel, S., Atanassov, P. & Kiefer, B. Catalytic activity of Co-Ni/C electrocatalysts for oxygen reduction reaction: a density functional theory study. *Phys. Chem. Chem. Phys.* **15**, 148–153 (2013).
- 17 Kattel, S. & Wang, G. Reaction pathway for oxygen reduction on FeN₄ embedded graphene. *J. Phys. Chem. Lett.* **5**, 452–456 (2014).
- 18 Orellana, V. Metal-phthalocyanine functionalized carbon nanotubes as catalyst for the oxygen reduction reaction: a theoretical study. *Chem. Phys. Lett.* **541**, 81–84 (2012).
- 19 Deng, D., Yu, L., Chen, X., Wang, G., Jin, L., Pan, X., Deng, J., Sun, G. & Bao, X. Iron encapsulated within pod-like carbon nanotubes for oxygen reduction reaction. *Angew. Chem. Int. Ed.* **52**, 371–375 (2013).
- 20 Chung, H. T., Won, J. H. & Zelenay, P. Active and stable carbon nanotube/nanoparticle composite electrocatalyst for oxygen reduction. *Nat. Commun.* **4**, 1922 (2013).
- 21 Hou, Y., Huang, T., Wen, Z., Mao, S., Cui, S. & Chen, J. Metal-organic framework-derived nitrogen-doped core-shell-structured porous Fe/Fe₃C@C nanoboxes supported on graphene sheets for efficient oxygen reduction reactions. *Adv. Energy Mater.* **4**, 1400337 (2014).
- 22 Hu, Y., Jensen, J. O., Zhang, W., Cleemann, L. N., Xing, W., Bjerrum, N. J. & Li, Q. Hollow spheres of iron carbide nanoparticles encased in graphitic layers as oxygen reduction catalysts. *Angew. Chem. Int. Ed.* **53**, 3675–3679 (2014).
- 23 Prasai, D., Tuberquia, J. C., Harl, R. R., Jennings, G. K. & Bolotin, K. I. Graphene: corrosion-inhibiting coating. *ACS Nano* **6**, 1102–1108 (2012).
- 24 Noh, S. H., Kwak, D. H., Seo, M. H., Ohsaka, T. & Han, B. First principles study of oxygen reduction reaction mechanisms on N-doped graphene with a transition metal support. *Electrochim. Acta* **140**, 225–231 (2014).
- 25 Noh, S. H., Seo, M. H., Ye, X., Makinose, Y., Okajima, T., Matsushita, N., Han, B. & Ohsaka, T. Design of an active and durable catalyst for oxygen reduction reactions using encapsulated Cu with N-doped carbon shells (Cu@N-C) activated by CO₂ treatment. *J. Mater. Chem. A* **3**, 22031–22034 (2015).
- 26 Chen, T. C., Zhao, M. Q., Zhang, Q., Tian, G. L., Huang, J. Q. & Wei, F. *In situ* monitoring the role of working metal catalyst nanoparticles for ultrahigh purity single-walled carbon nanotubes. *Adv. Funct. Mater.* **23**, 5066–5073 (2013).
- 27 Deng, J., Yu, L., Deng, D., Chen, X., Yang, F. & Bao, X. Highly active reduction of oxygen on a FeCo alloy catalyst encapsulated in pod-like carbon nanotubes with fewer walls. *J. Mater. Chem. A* **1**, 14868–14873 (2013).
- 28 Kresse, G. & Furthmüller, J. Efficient iterative schemes for ab initio total-energy calculations using a plane-wave basis set. *Phys. Rev. B* **54**, 11169 (1996).
- 29 Blöchl, P. E. Projector augmented-wave method. *Phys. Rev. B* **50**, 17953 (1994).
- 30 Tan, T. L., Wang, L.-L., Johnson, D. D. & Bai, K. A comprehensive search for stable Pt–Pd nanoalloy configurations and their use as tunable catalysts. *Nano Lett.* **12**, 4875–4880 (2012).
- 31 Zheng, Y., Jiao, Y., Zhu, Y., Li, L. H., Han, Y., Chen, Y., Du, A., Jaroniec, M. & Qiao, S. Z. Hydrogen evolution by a metal-free electrocatalyst. *Nat. Commun.* **5**, 3783 (2014).
- 32 Kumar, B., Asadi, M., Pisasale, D., Sinha-Ray, S., Rosen, B. A., Haasch, R., Abiade, J., Yarin, A. L. & Salehi-Khojin, A. Renewable and metal-free carbon nanofibre catalysts for carbon dioxide reduction. *Nat. Commun.* **4**, 2819 (2013).
- 33 Chen, Z., Dodelet, J.-P. & Zhang, J. *Non-Noble Metal Fuel Cell Catalysts* (John Wiley & Sons, 2014).
- 34 Kwak, D., Khetan, A., Noh, S., Pitsch, H. & Han, B. First principles study of morphology, doping level, and water solvation effects on the catalytic mechanism of nitrogen-doped graphene in the oxygen reduction reaction. *ChemCatChem* **6**, 2662–2670 (2014).
- 35 Lv, R., Li, Q., Botello-Méndez, A. R., Hayashi, T., Wang, B., Berkdemir, A., Hao, Q., Elias, A. L., Cruz-Silva, R. & Gutiérrez, H. R. Nitrogen-doped graphene: beyond single substitution and enhanced molecular sensing. *Sci. Rep.* **2**, 586 (2012).
- 36 Fujimoto, Y. & Saito, S. Formation, stabilities, and electronic properties of nitrogen defects in graphene. *Phys. Rev. B* **84**, 245446 (2011).
- 37 Hammer, B. & Nørskov, J. K. Theoretical surface science and catalysis—calculations and concepts. *Adv. Catal.* **45**, 71–129 (2000).
- 38 Nørskov, J. K., Rossmeisl, J., Logadottir, A., Lindqvist, L., Kitchin, J. R., Bligaard, T. & Jonsson, H. Origin of the overpotential for oxygen reduction at a fuel-cell cathode. *J. Phys. Chem. B* **108**, 17886–17892 (2004).
- 39 Greeley, J., Stephens, I., Bondarenko, A., Johansson, T. P., Hansen, H. A., Jaramillo, T., Rossmeisl, J., Chorkendorff, I. & Nørskov, J. K. Alloys of platinum and early transition metals as oxygen reduction electrocatalysts. *Nat. Chem.* **1**, 552–556 (2009).
- 40 Nørskov, J. K., Bligaard, T., Rossmeisl, J. & Christensen, C. H. Towards the computational design of solid catalysts. *Nat. Chem.* **1**, 37–46 (2009).
- 41 Stephens, I. E., Bondarenko, A. S., Grønberg, U., Rossmeisl, J. & Chorkendorff, I. Understanding the electrocatalysis of oxygen reduction on platinum and its alloys. *Energy Environ. Sci.* **5**, 6744–6762 (2012).
- 42 Bligaard, T. & Nørskov, J. K. Ligand effects in heterogeneous catalysis and electrochemistry. *Electrochim. Acta* **52**, 5512–5516 (2007).
- 43 Kim, H., Lee, K., Woo, S. I. & Jung, Y. On the mechanism of enhanced oxygen reduction reaction in nitrogen-doped graphene nanoribbons. *Phys. Chem. Chem. Phys.* **13**, 17505–17510 (2011).
- 44 Cui, X., Ren, P., Deng, D., Deng, J. & Bao, X. Single layer graphene encapsulating non-precious metals as high-performance electrocatalysts for water oxidation. *Energy Environ. Sci.* **9**, 123–129 (2016).
- 45 Tavakkoli, M., Kallio, T., Reynaud, A. G., Johans, C., Sainio, J., Jiang, H., Kauppinen, E. I. & Laasonen, K. Single-shell carbon-encapsulated iron nanoparticles: synthesis and high electrocatalytic activity for hydrogen evolution reaction. *Angew. Chem. Int. Ed.* **54**, 4535–4538 (2015).
- 46 Noh, S. H., Han, B. & Ohsaka, T. First-principles computational study of highly stable and active ternary PtCuNi nanocatalyst for oxygen reduction reaction. *Nano Res* **8**, 3394–3403 (2015).
- 47 Noh, S. H., Seo, M. H., Seo, J. K., Fischer, P. & Han, B. First principles computational study on the electrochemical stability of Pt–Co nanocatalysts. *Nanoscale* **5**, 8625–8633 (2013).
- 48 Nam, G., Park, J., Choi, M., Oh, P., Park, S., Kim, M. G., Park, N., Cho, J. & Lee, J.-S. Carbon-Coated Core–Shell Fe–Cu Nanoparticles as Highly Active and Durable Electrocatalysts for a Zn–Air Battery. *ACS Nano* **9**, 6493–6501 (2015).
- 49 Ramírez-Caballero, G. E., Ma, Y., Callejas-Tovar, R. & Balbuena, P. B. Surface segregation and stability of core-shell alloy catalysts for oxygen reduction in acid medium. *Phys. Chem. Chem. Phys.* **12**, 2209–2218 (2010).

- 50 Ma, Y. & Balbuena, P. B. Surface segregation in bimetallic Pt₃M (M = Fe, Co, Ni) alloys with adsorbed oxygen. *Surf. Sci.* **603**, 349–353 (2009).
- 51 Vitos, L., Ruban, A., Skriver, H. L. & Kollar, J. The surface energy of metals. *Surf. Sci.* **411**, 186–202 (1998).
- 52 Nørskov, J. K., Bligaard, T., Logadottir, A., Kitchin, J., Chen, J., Pandelov, S. & Stimming, U. Trends in the exchange current for hydrogen evolution. *J. Electrochem. Soc.* **152**, J23–J26 (2005).
- 53 Deng, J., Ren, P., Deng, D., Yu, L., Yang, F. & Bao, X. Highly active and durable non-precious-metal catalysts encapsulated in carbon nanotubes for hydrogen evolution reaction. *Energy Environ. Sci.* **7**, 1919–1923 (2014).
- 54 Deng, J., Ren, P., Deng, D. & Bao, X. Enhanced electron penetration through an ultrathin graphene layer for highly efficient catalysis of the hydrogen evolution reaction. *Angew. Chem. Int. Ed.* **54**, 2100–2104 (2015).



This work is licensed under a Creative Commons Attribution 4.0 International License. The images or other third party material in this article are included in the article's Creative Commons license, unless indicated otherwise in the credit line; if the material is not included under the Creative Commons license, users will need to obtain permission from the license holder to reproduce the material. To view a copy of this license, visit <http://creativecommons.org/licenses/by/4.0/>

© The Author(s) 2016

Supplementary Information accompanies the paper on the NPG Asia Materials website (<http://www.nature.com/am>)